ACS Combinatorial Science

Research Article

pubs.acs.org/acscombsci

High-Throughput Continuous Hydrothermal Synthesis of Nanomaterials (Part II): Unveiling the As-Prepared $Ce_xZr_yY_zO_{2-\delta}$ Phase Diagram

Raul Quesada-Cabrera,[†] Xiaole Weng,[‡] Geoff Hyett,[§] Robin J. H. Clark,[†] Xue Z. Wang,[∥] and Jawwad A. Darr*[,†]

[†]Department of Chemistry, University College London, Christopher Ingold Laboratories, 20 Gordon Street, London, WC1H 0AJ, United Kingdom

[‡]Department of Environmental Engineering, Zhejiang University, Zhejiang Province, Hangzhou, 310027, P. R. China

[§]Department of Chemistry, University of Southampton, Highfield, Southampton, SO17 1BJ, U.K.

[∥]Institute of Particle Science and Engineering, School of Process, Environmental and Materials Engineering, University of Leeds, Leeds LS2 9JT, United Kingdom

Supporting Information

ABSTRACT: High-throughput continuous hydrothermal flow synthesis was used to manufacture 66 unique nanostructured oxide samples in the Ce−Zr−Y−O system. This synthesis approach resulted in a significant increase in throughput compared to that of conventional batch or continuous hydrothermal synthesis methods. The as-prepared library samples were placed into a wellplate for both automated high-throughput powder X-ray diffraction and Raman spectroscopy data collection, which allowed comprehensive structural characterization and phase mapping. The data suggested that a continuous cubic-like phase field connects all three Ce−Zr−O, Ce−Y−O, and Y−Zr−O binary systems together with a smooth and steady transition between the structures of neighboring compositions. The continuous hydrothermal process led to as-prepared crystallite sizes in the range of 2−7 nm (as determined by using the Scherrer equation).

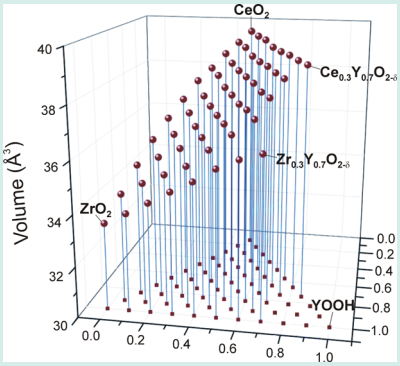

KEYWORDS: *high-throughput, hydrothermal synthesis, phase diagram, Raman spectroscopy, X-ray diffraction*

1. INTRODUCTION

Nanomaterials in the Ce−Zr−O, Y−Zr−O, and Ce−Y−O binary oxide systems are of interest for a broad range of applications, for example, catalyst supports for elimination of volatile organic compounds (VOCs),[1] electrolytes in intermediate-temperature solid-oxide fuel cells for stationary power applications,[2] three-way catalysts for cleanup of automotive gases,[3] homogeneous efficient fuel source in MO_x (mixed U/Pu oxide) nuclear reactors,[4] and phosphor materials (e.g. Y_2O_3:Eu^{3+}).[5]

Despite the importance of nanoceramics for technological applications, for example, as photocatalysts[6,7] or as battery or sensor materials,[8] rapid synthesis methods (within a day or less) to generate a large number of nanoceramics in significant quantities (typically 1 g or so) are still underdeveloped. Continuous hydrothermal flow synthesis (CHFS) technology is a rapid way to make nanomaterials and involves mixing a flow of supercritical water with a flow of aqueous metal salt solutions to give rapid nucleation and formation of nanoparticles.[6,7,9] The basic continuous hydrothermal technique has been developed independently by several groups. However, phase mapping using this technique remains relatively unexplored considering the vast literature on hydrothermal syntheses.[10] This is largely due to the greater availability of batch hydrothermal processing vessels, compared to the more complex CHFS equipment. Nevertheless, CHFS and related synthesis routes offer important advantages over batch methods, such as rapid nucleation, limited growth,[11] the ability to tune or control particle size and shape via changes in temperature/pressure/reagents,[12] and the advantage of producing many materials in a short time in the same apparatus, including the possible access to metastable phases.

Some of the authors of this work previously reported the development of a fully automated high-throughput continuous hydrothermal (HiTCH) process which was used for the production of a 66-sample nanoparticle $Ce_xZr_yY_zO_{2-\delta}$ library.[13] However, the phase diagram of the $Ce_xZr_yY_zO_{2-\delta}$ compounds was ascribed after post-treatment of the samples (1000 °C for 1 h in air) to enhance crystallization and promote the resolution of the X-ray diffraction data (during commissioning experiments for the I11 beamline at the Diamond Light Source, Rutherford Appleton Laboratory, Oxford).[14] In the current

Received: November 3, 2012
Revised: July 23, 2013
Published: August 1, 2013

   dx.doi.org/10.1021/co3001346 | ACS Comb. Sci. 2013, 15, 458−463

work, the implementation of high-throughput Raman spectroscopy allowed the investigation of the original as-prepared $Ce_xZr_yY_zO_{2-\delta}$ library. These data provided detailed information about the structural changes occurring across the entire $Ce_xZr_yY_zO_{2-\delta}$ map. Analysis of the extent of sintering of these nanoparticles upon heating has also been studied by comparing the crystallite sizes of the samples before and after heat treatment, as estimated using the Scherrer equation. To the best of our knowledge, this is the first comprehensive phase map to be reported for the low-temperature synthesis of $Ce_xZr_yY_zO_{2-\delta}$ nanoparticles, where some of the binary (such as $Ce_{0.2}Y_{0.8}O_{2-\delta}$ and $Ce_{0.1}Y_{0.9}O_{2-\delta}$) and ternary compositions (such as $Ce_{0.1}Zr_{0.3}Y_{0.6}O_{2-\delta}$) were hitherto unknown for as-prepared nanoparticles.

2. EXPERIMENTAL SECTION

2.1. Synthesis Method. A detailed description of the synthesis of the materials described here is given in the previous work.[13] Briefly, a manual high throughput continuous hydrothermal (HiTCH) flow synthesis system was used in which a superheated water feed at 450 °C and 24.1 MPa treated with a flow of appropriate premixed metal salt solutions to form nanoparticles. The precursor solutions were prepared from nitrate precursors (0.3 M $Y(NO_3)_3{\cdot}6H_2O$, 0.2 M $ZrO(NO_3)_2{\cdot}6H_2O$, and 0.3 M $(NH_4)_2Ce(NO_3)_6$). The nanoparticle slurries were cooled in flow via a pipe-in-pipe cooler and then the samples exited the process via a back-pressure regulator. Each mixture was fed in sequence with the system being purged with clean water between subsequent samples. Nominal values for metal ion content are used in the description of this work for simplicity instead of the actual compositions (Supporting Information Table S1 and Figure S1) determined by elemental analysis (EDX).[13] All slurries synthesized from the HiTCH system were dialyzed and freeze-dried at 12×10^{-3} Torr for 18 h. The powders from the 66 as-prepared samples were placed into an aluminum wellplate library in preparation for analysis.

2.2. High-Throughput Data Collection and Characterization. A data-mining method was introduced to cluster the large volume of XRD and Raman data collected into groups with similar diffraction/vibrational features. A widely used clustering algorithm K-means method was utilized herein, which has significantly accelerated the processing of the data analysis. Details of the clustering have been reported elsewhere.[15]

High-throughput powder X-ray diffraction (PXRD) was carried out for the as-prepared samples using a Bruker-AXS D8 (GADDS) diffractometer with Cu Kα radiation (λ = 0.15418 nm) at 40 kV and 150 mA over the 2θ range 20−70° with a step size of 0.02° per second. The diffractometer is equipped with an $x-y-z$ translational stage, which can be programmed to select each sample contained in a wellplate for data collection. The crystallite size was estimated from the XRD patterns using the Scherrer equation. The peak broadening because of instrumental contributions was determined using a 25 cm^2 alumina flat plate obtained from the National Institute of Standards and Technology (NIST) with peak intensities given by NIST and peak positions by the Inorganic Crystal Structure Database (ICSD). High-throughput Raman studies were conducted using a Renishaw InVia Raman microscope spectrometer equipped with a diode laser operating at 785 nm and position-sensitive detectors. The spectral resolution of the instrument was 1 cm^{-1}. All Raman spectra were recorded at room temperature, averaging 20 scans of 20 s each. For selected samples, Raman spectra were also recorded with a UV laser (325 nm) to distinguish the electronic features from vibrational bands.

3. RESULTS AND DISCUSSION

3.1. Phase Identification. The unequivocal assignment of nanocrystalline phases in the Ce−Zr−Y oxide system could not be established from XRD data alone in the case of the dominant cubic and tetragonal structures in the phase diagram because of broadening of the corresponding reflection peaks. For example, a gradual phase transition from cubic CeO_2 to tetragonal ZrO_2 should be expected upon incorporation of Zr atoms into the former structure (i.e. moving along the binary Ce−Zr oxide system), under the synthesis conditions employed here. However, the main indication of the substitution of Ce^{4+} by Zr^{4+} ions in these patterns is a peak shift related to their different sizes (Figure 1) and the presence of a tetragonal

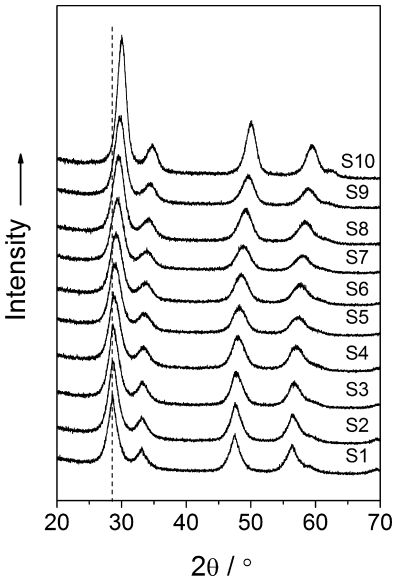

Figure 1. X-ray diffraction patterns from samples in the as-prepared Ce−Zr oxide binary system. All patterns could be refined using a cubic model, despite the presence of tetragonal phases identified using Raman spectroscopy. The peak shift highlighted is because of reduction of the unit cell volume upon substitution of Ce^{4+} with Zr^{4+} ions.

structure could only be clearly identified for those samples with very high Zr content (>80%), namely, $Ce_{0.1}Zr_{0.9}O_{2-\delta}$ (S10 in Figure 2) and pure ZrO_2 (S11). Nevertheless, the implementation of high-throughput Raman spectroscopy as a complementary technique allowed rapid identification of the predominant phases in the system (Figure 3). The Raman spectra and main band modes of all 66 samples in this study are shown in Supporting Information Figure S1 and Table S2, respectively.

The Raman spectrum of the as-prepared cubic CeO_2 phase ($Fm\bar{3}m$) is dominated by a single broad F_{2g} band (symmetric Ce−O stretching vibrations of the fluorite structure) at 465 cm^{-1} for bulk ceria, but its wavenumber, shape and intensity are very sensitive to particle size and to defects related to oxygen vacancies, strain and phonon confinement.[16] In the case of our nanostructured CeO_2 sample, the band was observed at 458 cm^{-1} (Figure 3a). The introduction of relatively small amounts of Zr^{4+} ions (<40 at.%) in the CeO_2 structure results in a

dx.doi.org/10.1021/co3001346 | ACS Comb. Sci. 2013, 15, 458−463

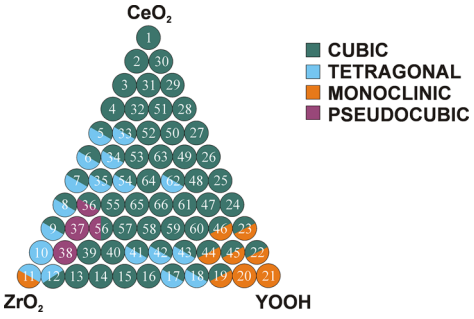

Figure 2. Phase diagram of the 66 samples in the as-prepared Ce−Zr−Y oxide system as suggested from high-throughput Raman spectroscopy.

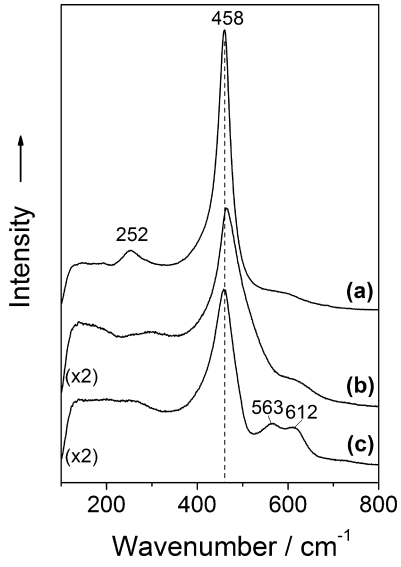

Figure 3. Raman spectra of (a) pure CeO_2 (S1), (b) $Ce_{0.6}Zr_{0.4}O_2$ (S5), and (c) $Ce_{0.6}Y_{0.4}O_2$ (S27).

metal−oxygen bond length shortening and a consequent shift of the F_{2g} band from 458 to 464 cm^{-1} (Figure 3b). In contrast, the substitution of Ce^{4+} ions by Y^{3+} ions with similar ionic radii along the Ce−Y oxide binary system did not affect the wavenumber of the main F_{2g} band even for Y contents below 80 at.% (Figure 3c). Nevertheless, the ionic substitution in the CeO_2 structure results in the appearance of extra bands in the spectrum. In general, broad bands below 400 cm^{-1} and in the range 500−600 cm^{-1} are related to oxygen vacancies and dopant defects. In particular, the presence of a relatively intense broad band at ∼252 cm^{-1} has been associated with the displacement of oxygen atoms from the ideal fluorite lattice (Figure 3a).[17] The additional bands observed at 563 and 612 cm^{-1} in Figure 3c are due to oxygen vacancies (charge valence in the Ce^{4+}/Y^{3+} substitution) and metal substitution, respectively.[18] Above 30 at.% Zr content in the Ce−Zr oxide binary system, the presence of a tetragonal structure is gradually envisaged by changes in the shape and intensity of the F_{2g} band, together with the appearance of a broad band around 145 cm^{-1} and bands in the range 1200−1800 cm^{-1} (Supporting Information Figure S2).[19] The F_{2g} band is still the dominant feature below 80 at.% Zr content, thus, coexistence between tetragonal and cubic phases can be assumed. However, progressively higher concentrations of Zr atoms in the structure finally result in a pure tetragonal $Ce_{0.1}Zr_{0.9}O_{2-\delta}$ (S10) phase (Figure 4a). Six Raman-active modes (A_{1g} + $3E_g$ + $2B_{1g}$) are predicted for the tetragonal $P4_2/nmc$ structure, however, only

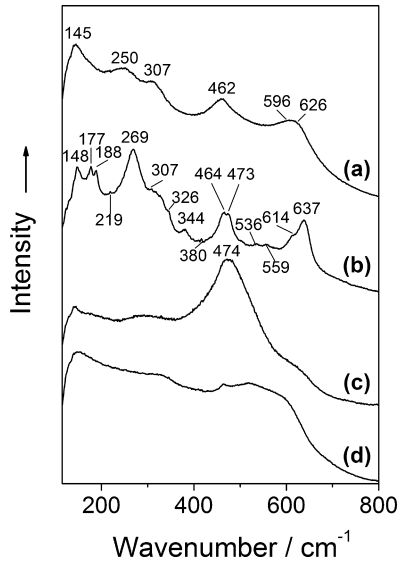

Figure 4. Raman spectra of (a) tetragonal $Ce_{0.1}Zr_{0.9}O_{2-\delta}$ (S10), (b) tetragonal/monoclinic ZrO_2 (S11), (c) cubic/tetragonal $Ce_{0.4}Zr_{0.5}Y_{0.1}O_{2-\delta}$ (S35), and (d) pseudocubic $Ce_{0.1}Zr_{0.8}Y_{0.1}O_{2-\delta}$ (S38).

five are usually observed since the bands at 596 and 626 cm^{-1} typically overlap.[20] The wavenumbers of these bands vary with Zr content and particle size. In the Raman spectra of pure tetragonal phases, the F_{2g} band (462 cm^{-1}) should be weaker than that at 307 cm^{-1} as it is shown in Figure 4a.[21] Finally, all Raman-active bands predicted for tetragonal ($P4_2/nmc$, A_{1g}+$3E_g$+$2B_{1g}$) and monoclinic ($P2_1/c$, $9A_g$ + $9B_g$) phases were identified in the Raman spectrum of pure ZrO_2 (S11) (Figure 4b). Most of these bands overlap, but some are specific to each structure.[22] Coexistence of both tetragonal and cubic phases was suggested in the binary Zr−Y oxide system for structures with low and high Y content, such as $Zr_{0.9}Y_{0.1}O_{2-\delta}$ (S12) and $Zr_{0.4}Y_{0.6}O_{2-\delta}$ (S17) (Figure 5a), which is in agreement with the report by Yashima et al.[23] At intermediate Y atomic contents, for example, $Zr_{0.8}Y_{0.2}O_{2-\delta}$ (S13), $Zr_{0.7}Y_{0.3}O_{2-\delta}$ (S14), etc., only cubic phases were suggested with a strong F_{2g} band located in the range ∼600−620 cm^{-1} (Figure 5b).[24] All Raman spectra of samples with high Y content (>70−80 at.%) showed evidence of a monoclinic YOOH phase (Supporting Information Figure S2). The pure monoclinic YOOH structure ($P2_1/m$) is characterized by nine Raman-active modes ($6A_g$ + $3B_g$) (Figure 5c). Among the ternary Ce−Zr−Y oxide samples, the predominant phase was cubic and in a few cases this was in coexistence with a (metastable) tetragonal structure, for example, sample $Ce_{0.4}Zr_{0.5}Y_{0.1}O_{2-\delta}$ (S35) (Figure 4c). However, it was interesting to observe the presence of single-phase pseudocubic structures in nominal compositions such as $Ce_{0.1}Zr_{0.8}Y_{0.1}O_{2-\delta}$ (S38) (Figure 4d).

When the entire phase diagram is viewed as a whole (Figure 2), there appears to be a continuous solid solution of cubic or pseudocubic phases that pervades the entire phase diagram, connecting each oxide binary system together by means of ternary compositions.

dx.doi.org/10.1021/co3001346 | ACS Comb. Sci. 2013, 15, 458−463

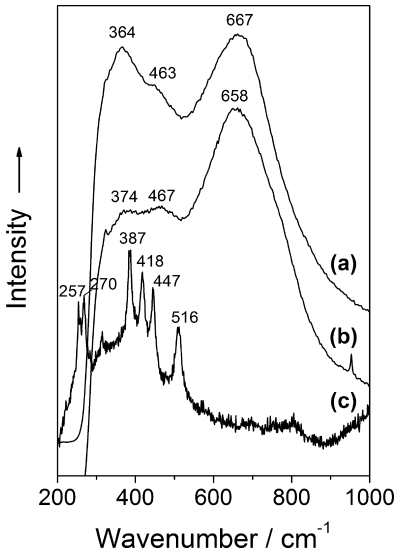

Figure 5. Raman spectra of (a) tetragonal/cubic $Zr_{0.4}Y_{0.6}O_{2-\delta}$ (S17), (b) cubic $Zr_{0.6}Y_{0.4}O_{2-\delta}$ (S15), and (c) monoclinic YOOH (S21).

3.2. Sintering of Nanoparticles. Taking into consideration the limitations of the XRD data, a cubic structure was initially modeled for the extensive and continuous phase field which extended across the entire sample map, except for the clearly tetragonal phases mentioned (S10 and S11) to have a rough estimate of the variation in crystallite size within samples (Figure 6). Some samples containing a high concentration of yttrium, namely S17−S23 and S44−S46, were mixtures of cubic and YOOH phases and could not be refined. Those samples were excluded from the analysis. The crystallite size was roughly estimated using the Scherrer equation from the value obtained for the *a* parameter in the refinements of the cubic model (or tetragonal model in the case of S10 and S11). On the basis of crystallite size, the as-prepared 66 samples seem to be within the range of 2−7 nm, apparently distributed into three distinct regions (Figure 6a). The compounds in the top half of the phase diagram (high Ce concentration) seem to have crystallite sizes in the range 3.5−4.5 nm, whereas those in the bottom half of the diagram are larger at 5−7 nm. A few samples, particularly those with similar atomic ratios of Ce and Y in the Ce−Y−O binary system, had crystallite sizes in the range ∼2.0−3.5 nm (Figure 7a). Despite these apparent groups, any changes in crystallite size appear to show a smooth transition between neighboring samples, which suggests that the factors controlling their size are subtle and largely down to small changes in composition. A smooth transition in unit cell volume upon changes in composition was also observed in Figure 6. The ionic radii of both Ce^{4+} and Y^{3+} ions are very similar (0.97 and 1.01 Å, respectively), whereas Zr^{4+} ions are substantially smaller (0.87 Å), resulting in unit cell volumes that drop gradually toward the ZrO_2 corner of the diagram (Figure 6).

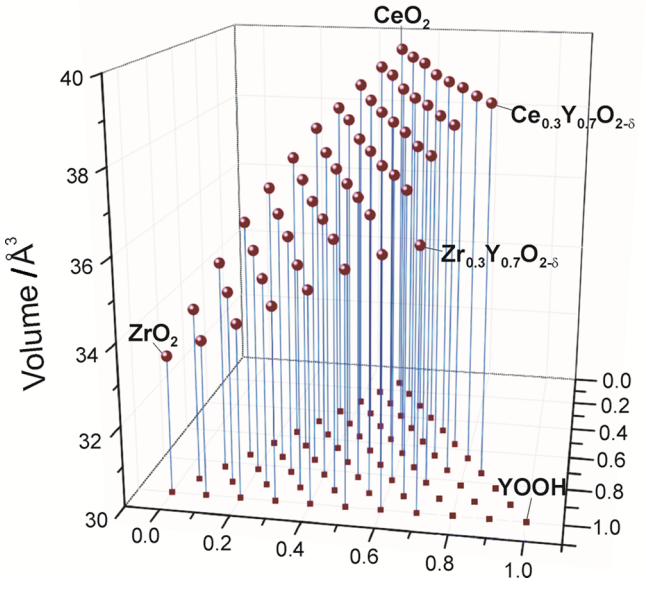

Figure 6. Estimated unit cell volume from the X-ray diffraction data refined using a cubic structure model for all samples except for pure ZrO_2 (S11) and $Ce_{0.1}Zr_{0.9}O_{2-\delta}$ (S10) that were clearly tetragonal (according to X-ray data alone). Note in samples containing mixtures of phases, only the major phase was analyzed. The X-ray patterns from the samples with high content of Y could not be refined and are not included in the graph.

Some of the authors involved in the current work previously reported high-quality XRD data of the same library after heat treatment at 1000 °C for 1 h. With the new XRD data herein, it has now been possible to assess the size of the nanoparticles before heat-treatment (Supporting Information Table S3). The difference between crystallite size estimated before and after the heat treatment is represented by the darkness of the spheres in the schematic diagram in Figure 7b. The size of each sphere correlates with the size of the as-prepared samples. A few samples, such as CeO_2 (S1), $Ce_{0.9}Zr_{0.1}O_{2-\delta}$ (S2), etc., are represented in black or dark gray in the figure; these samples underwent extensive sintering during the heat treatment. Nevertheless, it can be observed that most of the samples did not experience severe sintering after heating at 1000 °C for 1 h (Figure 7b).

4. CONCLUSIONS AND OUTLOOK FOR FUTURE RESEARCH

An entire as-prepared Ce−Zr−Y ternary oxide nanoparticle phase map has been investigated through the high-throughput complementary techniques of X-ray diffraction and Raman spectroscopy. The nanomaterials were made at relatively low temperatures (certainly none of the nanomaterials referred to herein was exposed to temperatures over 400 °C during synthesis) using a high-throughput CHFS method. Importantly, when compared to our previous report on the samples after heat treatment, this report highlighted that changes in unit cell volume, sintering behavior, initial particle size and phase behavior changed gradually because of the consistency of conditions offered by the HiTCH synthesis method. In CHFS, the particle properties appear to be largely from changes in elemental composition and therefore this dictates solubility and formation in a subtle way across the phase diagram. Further, comparison of crystallite sizes (via analysis of the XRD peak widths and application of the Scherrer equation) before and after heating to 1000 °C for 1 h, revealed that particle growth and sintering were most severe at the corners of the phase diagram and were substantially reduced toward the center of the phase diagram.

While the development of high-throughput CHFS (HiTCH) has allowed rapid production of many samples in a relatively short space of time, if any key materials identified from such libraries are to reach commercial interest, it will also be

dx.doi.org/10.1021/co3001346 | ACS Comb. Sci. 2013, 15, 458−463

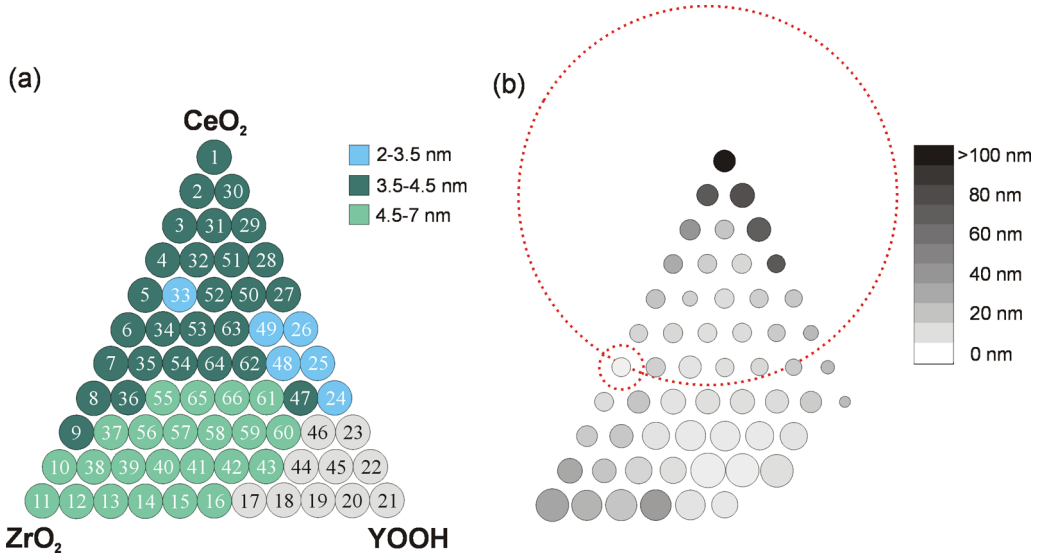

Figure 7. (a) Position of the 66 samples in the Ce−Zr−Y oxide system. The color code highlights the different range of crystallite sizes (Scherrer) of the as-prepared samples. The samples with high Y content (gray spheres) were varying mixtures of apparently cubic and YOOH phases and have been excluded from the analyses. (b) Schematic diagram illustrating the relative crystallite size of the 66 samples before and after heat treatment (1000 °C for 1 h, ref 13). The relative crystallite size estimated for the as-prepared samples correlates with the size of the spheres shown, whereas their gray scale indicates the degree of sintering after the heat-treatment (i.e., the difference in crystallite size). The degree of sintering is also highlighted by the two red dashed circles that illustrate the size of two stereotypical samples (S2 and S7) after the heat treatment. A full explanation is described in Supporting Information. The negligible sintering of the nanoparticles in sample S7 contrasts with the drastic change in crystallite size of sample S2 upon heat-treatment.

important to scale up CHFS technology. Toward this end, the authors have recently developed a pilot plant scale CHFS, which uses a new mixer design and is capable of producing >1 kg per hour of nanomaterials (×800 scale-up) with similar characteristics to those obtained in the lab-scale reactors.[25] Thus, the benefit of high throughput synthesis and characterization and then rapid scale-up production for nanoceramics are within grasp of researchers.

■ ASSOCIATED CONTENT

Supporting Information

Raman spectra of the entire Ce−Zr−Y−O phase diagram and unit cell parameters and crystallite sizes for the 66 samples before and after heat treatment. This material is available free of charge via the Internet at http://pubs.acs.org.

■ AUTHOR INFORMATION

Corresponding Author

*Fax: +44 (0)20 7679 7463. Tel: +44 (0)20 7679 4345. E-mail: j.a.darr@ucl.ac.uk.

Author Contributions

The manuscript was written through contributions of all authors. All authors have given approval to the final version of the manuscript.

Notes

The authors declare no competing financial interest.

■ ACKNOWLEDGMENTS

The authors thank Dr. Sonal Brown for assistance in Raman data collection. J.A.D. and R.Q.C. were funded by EPSRC under "Continuous Hydrothermal Synthesis of Nanomaterials: From Laboratory to Pilot Plant" [EP/E040551/1]. X.W. was financially supported by Zhejiang Provincial Natural Science Foundation of China (LQ12E08011) and The National Natural Science Fundation of China (Grant No. 51208458).

■ REFERENCES

(1) Trovarelli, A.; Boaro, M.; Rocchini, E.; Leitenburg, C.; Dolcetti, G. Some recent developments in the characterization of Ce-based catalysts. *J. Alloys Compd.* **2001**, *323*−*324*, 584−591. Cales, B.; Baumard, J. F. Mixed conduction and defect structure of ZrO_2−CeO_2−Y_2O_3 solid solutions. *J. Electrochem. Soc.* **1984**, *131*, 12407−2413.

(2) Goodenough, J. B. Ceramic technology: Oxide-ion conductors by design. *Nature* **2000**, *404*, 821−823.

(3) Wright, C. S.; Walton, R. I.; Thompsett, D.; Fisher, J.; Ashbrook, S. E. One-step hydrothermal synthesis of nanocrystalline ceria−zirconia mixed oxides: The beneficial effect of sodium inclusion on redox properties. *Adv. Mater.* **2007**, *19*, 4500−4504.

(4) Martin, P.; Grandjean, S.; Valot, C.; Carlot, G.; Ripert, M.; Blanc, P.; Hennig, C. XAS study of $(U_{1-y}Pu_y)O_2$ solid solutions. *J. Alloys Compd.* **2007**, *444*, 410−414.

(5) Xiao, Y.; Wu, D. P.; Jiang, Y.; Liu, N.; Liu, J. L.; Jiang, K. Nano-sized Y_2O_3:Eu^{3+} hollow spheres with enhanced photoluminescence properties. *J. Alloys Compd.* **2011**, *509*, 5755−5760.

(6) Thompson, K.; Goodall, J.; Kellici, S.; Mattinson, J. A.; Egerton, T. A.; Rehman, I.; Darr, J. A. Screening tests for the evaluation of nanoparticle titania photocatalysts. *J. Chem. Technol. Biotechnol.* **2009**, *84*, 1717−1725.

(7) Zhang, Z.; Goodall, J.; Brown, S.; Karlsson, L.; Clark, R. J. H.; Hutchison, J. L.; Rehman, I. U.; Darr, J. A. Continuous hydrothermal synthesis of extensive 2D sodium titanate ($Na_2Ti_3O_7$) nano-sheets. *Dalton Trans.* **2010**, *39*, 711−714.

(8) Elouali, S.; Bloor, L. G.; Binions, R.; Parkin, I. P.; Carmalt, C. J.; Darr, J. A. Gas sensing with nano-indium oxides (In_2O_3) prepared via continuous hydrothermal flow synthesis. *Langmuir* **2012**, *28*, 1879−1885.

(9) Darr, J. A.; Poliakoff, M. New directions in inorganic and metal−organic coordination chemistry in supercritical fluids. *Chem. Rev.* **1999**, *99*, 495−541. Cabañas, A.; Darr, J. A.; Lester, E.; Poliakoff, M. A continuous and clean one-step synthesis of nano-particulate

$Ce_{1-x}Zr_xO_2$ solid solutions in near-critical water. *Chem. Commun.* **2000**, *11*, 901−902. Cabañas, A.; Darr, J. A.; Lester, E.; Poliakoff, M. Continuous hydrothermal synthesis of inorganic materials in a near-critical water flow reactor; the one-step synthesis of nano-particulate $Ce_{1-x}Zr_xO_2$ (x = 0−1) solid solutions. *J. Mater. Chem.* **2001**, *11*, 561−568. Chaudhry, A. A.; Haque, S.; Kellici, S.; Boldrin, P.; Rehman, I.; Fazal, A. K.; Darr, J. A. Instant nano-hydroxyapatite: a continuous and rapid hydrothermal synthesis. *Chem. Commun.* **2006**, *21*, 2286−2288. Chaudhry, A. A.; Goodall, J.; Vickers, M.; Cockcroft, J. K.; Rehman, I.; Knowles, J. C.; Darr, J. A. Synthesis and characterisation of magnesium substituted calcium phosphate bioceramic nanoparticles made via continuous hydrothermal flow synthesis. *J. Mater. Chem.* **2008**, *18*, 5900−5908. Chaudhry, A. A.; Yan, H.; Gong, K.; Inam, F.; Viola, G.; Reece, M. J.; Goodall, J. B.; Rehman, I.; McNeil-Watson, F. K.; Corbett, J. C.; Knowles, J. C.; Darr, J. A. High-strength nanograined and translucent hydroxyapatite monoliths via continuous hydrothermal synthesis and optimized spark plasma sintering. *Acta Biomater.* **2010**, *7*, 791−799. Gruar, R.; Tighe, C. J.; Reilly, L. M.; Sankar, G.; Darr, J. A. Tunable and rapid crystallisation of phase pure Bi_2MoO_6 (koechlinite) and $Bi_2Mo_3O_{12}$ via continuous hydrothermal synthesis. *Solid State Sci.* **2010**, *12*, 1683−1686. Boldrin, P.; Hebb, A. K.; Chaudhry, A. A.; Otley, L.; Thiebaut, B.; Bishop, P.; Darr, J. A. Direct synthesis of nanosized $NiCo_2O_4$ spinel and related compounds via continuous hydrothermal synthesis methods. *Ind. Eng. Chem. Res.* **2007**, *46*, 4830−4838. Weng, X.; Brett, D.; Yufit, V.; Shearing, P.; Brandon, N.; Reece, M.; Yan, H.; Tighe, C. J.; Darr, J. A. Highly conductive low nickel content nano-composite dense cermets from nano-powders made via a continuous hydrothermal synthesis route. *Solid State Ion.* **2010**, *181*, 827−834. Weng, X. L.; Boldrin, P.; Abrahams, I.; Skinner, S. J; Darr, J. A. Direct syntheses of mixed ion and electronic conductors $La_4Ni_3O_{10}$ and $La_3Ni_2O_7$ from nanosized coprecipitates. *Chem. Mater.* **2007**, *19*, 4382−4384. Weng, X. L.; Boldrin, P.; Abrahams, I.; Skinner, S. J.; Kellici, S.; Darr, J. A. Direct syntheses of $La_{n+1}Ni_nO_{3n+1}$ phases (n = 1, 2, 3 and infinity) from nanosized co-crystallites. *J. Solid State Chem.* **2008**, *181*, 1123−1132. Weng, X. L.; Perston, B.; Wang, X. Z.; Abrahams, I.; Lin, T.; Yang, S. F.; Evans, J. R. G.; Morgan, D. J.; Carley, A. F.; Bowker, M.; Knowles, J. C.; Rehman, I.; Darr, J. A. Synthesis and characterization of doped nano-sized ceria-zirconia solid solutions. *Appl. Catal,. B* **2009**, *90*, 405−415. Weng, X. L.; Zhang, J. Y.; Wu, Z. B.; Liu, Y.; Wang, H. Q.; Darr, J. A. Continuous hydrothermal syntheses of highly active composite nanocatalysts. *Green Chem.* **2011**, *13*, 850−853.

(10) Adschiri, T. Supercritical hydrothermal synthesis of organic-inorganic hybrid nanoparticles. *Chem. Lett.* **2007**, *36*, 1188−1193. Takami, S.; Sato, T.; Mousavand, T.; Ohara, S.; Umetsu, M.; Adschiri, T. Hydrothermal synthesis of surface-modified iron oxide nanoparticles. *Mater. Lett.* **2007**, *61*, 4769−4772.

(11) Kanamura, K.; Goto, A.; Ho, R. Y.; Umegaki, T.; Toyoshima, K.; Okada, K.; Hakuta, Y.; Adschiri, T.; Arai, K. Preparation and electrochemical characterization of $LiCoO_2$ particles prepared by supercritical water synthesis. *Electrochem. Solid State Lett.* **2000**, *3*, 256−258. Ohara, S.; Mousavand, T.; Umetsu, M.; Takami, S.; Adschiri, T.; Kuroki, Y.; Takata, M. Hydrothermal synthesis of fine zinc oxide particles under supercritical conditions. *Solid State Ion.* **2004**, *172*, 261−264.

(12) Sue, K.; Hakuta, Y.; Smith, R. L.; Adschiri, T.; Arai, K. Solubility of lead(II) oxide and copper(II) oxide in subcritical and supercritical water. *J. Chem. Eng. Data* **1994**, *44*, 1422−1426.

(13) Weng, X. L.; Cockcroft, J. K.; Hyett, G.; Vickers, M.; Boldrin, P.; Tang, C. C.; Thompson, S. P.; Parker, J. E.; Knowles, J. C.; Rehman, I.; Parkin, I.; Evans, J. R. G.; Darr, J. A. High-throughput continuous hydrothermal synthesis of an entire nanoceramic phase diagram. *J. Comb. Chem.* **2009**, *11*, 829−834.

(14) Parker, J. E.; Thompson, S. P.; Cobb, T. M.; Yuan, F. J.; Potter, J.; Lennie, A. R.; Alexander, S.; Tighe, C. J.; Darr, J. A; Cockcroft, J. C; Tang, C. C. High-throughput powder diffraction on beamline I11 at Diamond. *J. Appl. Crystallogr.* **2011**, *44*, 102−110.

(15) Yang, Y.; Lin, T. A.; Weng, X. L.; Darr, J. A.; Wang, X. Z. Data flow modeling, data mining and QSAR in high-throughput discovery of functional nanomaterials. *Comput. Chem. Eng.* **2011**, *35*, 671−678.

(16) Weber, W. H.; Hass, K. C.; McBride, J. R. Raman study of CeO_2: Second-order scattering, lattice dynamics, and particle-size effects. *Phys. Rev. B* **1993**, *48*, 178−185. Chiang, Y. M.; Lavik, E. B.; Kosacki, I.; Tuller, H. L.; Ying, J. Y. Defect and transport properties of nanocrystalline CeO_2. *Appl. Phys. Lett.* **1996**, *69*, 185−187. Gouadec, G.; Colomban, P. Raman Spectroscopy of nanomaterials: How spectra relate to disorder, particle size and mechanical properties. *Prog. Cryst. Growth Charact. Mater.* **2007**, *53*, 1−56. Spanier, J. E.; Robinson, R. D.; Zhang, F.; Chan, S. W.; Herman, I. P. Size-dependent properties of CeO_{2-y} nanoparticles as studied by Raman scattering. *Phys. Rev. B* **2001**, *64*, 245407−245415.

(17) Vidal, H.; Kaspar, J.; Pijolat, M.; Colon, G.; Bernal, S.; Cordon, A.; Perrichon, V.; Fally, F. Redox behavior of CeO_2−ZrO_2 mixed oxides: I. Influence of redox treatments on high surface area catalysts. *Appl. Catal., B* **2000**, *27*, 49−63.

(18) Nakajima, A.; Yoshihara, A.; Ishigame, M. Defect-induced Raman spectra in doped CeO_2. *Phys. Rev. B* **1994**, *50* (18), 13297−13307.

(19) Yashima, M.; Arashi, H.; Kakihana, M.; Yoshimura, M. Raman scattering study of cubic−tetragonal phase transition in $Zr_{1-x}Ce_xO_2$ solid solution. *J. Am. Ceram. Soc.* **1994**, *77*, 1067−1071. Yashima, M.; Kakihana, M.; Yoshimura, M. Metastable-stable phase diagrams in the zirconia-containing systems utilized in solid-oxide fuel cell application. *Solid State Ion.* **1996**, *86*−*88*, 1131−1149. Kaspar, J.; Fornasiero, P.; Balducci, G.; Di Monte, R.; Hickey, N.; Sergo, V. Effect of ZrO_2 content on textural and structural properties of CeO_2−ZrO_2 solid solutions made by citrate complexation route. *Inorg. Chim. Acta* **2003**, *349*, 217−226.

(20) Hirata, T.; Asari, E.; Kitajima, M. Infrared and Raman spectroscopic studies of ZrO_2 polymorphs doped with Y_2O_3 or CeO_2. *J. Solid State Chem.* **1994**, *110*, 201−207.

(21) Zhang, F.; Chen, C. H.; Hanson, J. C.; Robinson, R. D.; Herman, I. P.; Chan, S. W. Phases in ceria−zirconia binary oxide (1−x)$CeO_{2-x}ZrO_2$ nanoparticles: The effect of particle size. *J. Am. Ceram. Soc.* **2006**, *89*, 1028−1036.

(22) Philippi, C. M.; Mazdiyasni, S. Infrared and raman spectra of zirconia polymorphs. *J. Am. Ceram. Soc.* **1971**, *54*, 254−258. Anastassakis, E.; Papanicolaou, B.; Asher, I. M. Lattice dynamics and light scattering in Hafnia and Zirconia. *J. Phys. Chem. Solids* **1975**, *36*, 667−676. Siu, G. G.; Stokes, M. J.; Liu, Y. Variation of fundamental and higher-order Raman spectra of ZrO_2 nanograins with annealing temperature. *Phys. Rev. B* **1999**, *59*, 3173−3179.

(23) Yashima, M.; Ohtake, K.; Kakihana, M.; Arashi, H.; Yoshimura, M. Determination of tetragonal-cubic phase boundary of $Zr_{1-x}R_xO_{2-x/2}$ (R = Nd, Sm, Y, Er, Yb) by Raman scattering. *J. Phys. Chem. Solids* **1996**, *57*, 17−24.

(24) Feinberg, A.; Perry, C. H. Structural disorder and phase transitions in ZrO_2−Y_2O_3 system. *J. Phys. Chem. Solids* **1981**, *42*, 513−518.

(25) Tighe, C. J.; Quesada Cabrera, R.; Gruar, R.; Darr, J. A. Scale-up production of nanoparticles: continuous supercritical water synthesis of Ce−Zn oxides. *Ind. Eng. Chem. Res.* **2013**, *52*, 5522−5528.